

Effects of tool edge radius on ductile machining of silicon: an investigation by FEM

This content has been downloaded from IOPscience. Please scroll down to see the full text.

2009 Semicond. Sci. Technol. 24 075018

(<http://iopscience.iop.org/0268-1242/24/7/075018>)

View [the table of contents for this issue](#), or go to the [journal homepage](#) for more

Download details:

IP Address: 131.113.58.246

This content was downloaded on 26/06/2015 at 08:10

Please note that [terms and conditions apply](#).

Effects of tool edge radius on ductile machining of silicon: an investigation by FEM

Jiwang Yan¹, Hongwei Zhao² and Tsunemoto Kuriyagawa¹

¹ Department of Nanomechanics, Graduate School of Engineering, Tohoku University, Aramaki Aoba 6-6-01, Aoba-ku, Sendai, 980-8579, Japan

² School of Mechanical Science and Engineering, Nanling Campus, Jilin University, Changchun, Jilin 130025, People's Republic of China

E-mail: yanjw@pm.mech.tohoku.ac.jp

Received 19 January 2009, in final form 21 April 2009

Published 9 June 2009

Online at stacks.iop.org/SST/24/075018

Abstract

The submicron-level orthogonal cutting process of silicon has been investigated by the finite element approach, and the effects of tool edge radius on cutting force, cutting stress, temperature and chip formation were investigated. The results indicate that increasing the tool edge radius causes a significant increase in thrust force and a decrease in chip thickness. A hydrostatic pressure (~ 15 GPa) is generated in the cutting region, which is sufficiently high to cause phase transformations in silicon. The volume of the material under high pressure increases with the edge radius. Temperature rise occurs intensively near the tool–chip interface while the highest cutting temperature (~ 300 °C) is far lower than the necessary temperature for activating dislocations in silicon. As the edge radius is beyond a critical value (~ 200 nm), the primary high-temperature zone shifts from the rake face side to the flank face side, causing a transition in the tool wear pattern from crater wear to flank wear. The simulation results from the present study could successfully explain existing experimental phenomena, and are helpful for optimizing tool geometry design in silicon machining.

(Some figures in this article are in colour only in the electronic version)

1. Introduction

Single-crystal silicon is one of the most popular semiconductor materials for manufacturing electronic products and micro-electro mechanical systems (MEMS). Silicon is also an important optical material for infrared lenses in thermal imaging and night-vision systems. For this reason, ultraprecision machining of silicon has become a focused research area in recent years. A lot of experimental studies have been carried out on the topic of ‘ductile machining’ of silicon [1–6]. These studies have demonstrated that although silicon is a nominally hard and brittle material, it can be machined in a completely ductile manner at an extremely small machining scale down to the submicron level, yielding continuous chips and smooth surfaces. Researchers have also found that silicon undergoes high-pressure phase

transformation during ductile machining, leaving a near-surface layer of an amorphous structure [7–12].

In silicon machining, improving ductile machinability and eliminating subsurface damage are two important tasks. The fundamental machining mechanisms, including the effects of tool edge geometry, cutting speed and environment on silicon machining, are very complicated and have not yet been completely clarified. There are distinct differences and even contradictions among results reported by different research groups. One of the controversial issues is the effect of tool rake angle and tool edge radius. While it is widely accepted that an intermediate negative rake angle from -20 to -50° is beneficial for ductile machining [1–6] and an extremely high negative rake angle from -60 to -80° obstructs material removal [13, 14]; a few authors reported that ductile cutting of silicon is achievable even at a -80° rake angle [15]. As for tool edge radius, while it is widely accepted that a sharp

tool is beneficial; some researchers reported that a blunt tool, if its edge radius is below an upper bound (700–800 nm), is helpful for ductile machining [16, 17]. They experimentally found that the larger the cutting edge radius is, the larger the critical undeformed chip thickness is [17].

There might be many reasons causing the data inconsistency, such as experimental errors resulting from machine deflections (which make the actual depth of cut different from the desired value), tool vibration, environmental changes, tool wear (which makes the actual tool geometry different from the initial one), as well as differences in evaluation and measurement methods. Also, it is still technologically impossible to examine the effect of a single factor while keeping other factors completely the same. For this reason, it is expected that the simulation approach may assist in understanding the machining mechanism. Visualization of cutting stress, cutting temperature and chip formation behavior should be helpful for optimizing the machining process.

Molecule dynamics (MD) has been used in a few previous studies to simulate the cutting mechanism of silicon. However, due to the limitations in computational ability, the machining scale simulated by MD is currently limited to the nanometer level, far smaller than the practical machining scale in manufacturing applications. Practically, for achieving a high material removal rate, undeformed chip thickness is usually set in a range from a few tens of nanometers to the submicron level [1–6].

An alternative method to simulate a ductile machining process would be the finite element method (FEM). FEM has been used to simulate the cutting processes of various materials such as aluminum, steel and alloys in previous studies from several decades ago [18–24]. In most of the previous studies, the machining scale was in millimeter or submillimeter level. Recently, a few commercially available FEM codes have been developed which can be used to simulate micro/nano cutting. These programs enable two- or three-dimensional simulations with coupled thermo-mechanical analysis. Also, chip formation and chip separation from the workpiece can be realized by element remeshing techniques, rather than the conventional compulsory separation techniques. For example, Woon *et al* recently performed FEM simulation of micro-machining of the AISI 4340 steel using the ABAQUS suite of software, and investigated the effects of the ratio of undeformed chip thickness and edge radius on stress distribution in the cutting region [25].

In the present paper, we carried out FEM simulations of silicon cutting at the practically important submicron scale and investigated changes in chip formation behavior, cutting forces, stress distribution and temperature distribution in the cutting region when the tool edge radius was changed. It is expected that by visualizing these important parameters of the micro-cutting process, this study could provide some insights into the changes in the cutting mechanism with tool edge geometry.

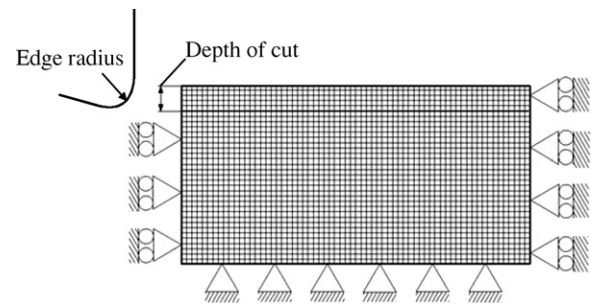


Figure 1. FEM simulation model.

2. Simulation procedures

2.1. The cutting model and boundary conditions

A commercially available FEM program Marc, produced by the MSC Software Corporation, was used as a simulation core. Marc is a nonlinear FEM program and enables us to study the performance of a part undergoing large permanent deformations and part-to-part contact problems. The program was operated by combining with a pre/post-processor Mentat.

Figure 1 shows an FE cutting model we used in this work. We used plane-strain conditions to simulate a two-dimensional orthogonal cutting process. The model is composed of a deformable workpiece and a rigid cutting tool. The width and the thickness of the workpiece are 1200 nm and 600 nm, respectively. The workpiece was constructed by bilinear quadrilateral elements. Initial elements number was 600 in total.

Rigid walls were used as the workpiece boundaries. To use rigid walls is because silicon is a hard and rigid material, and the cutting point is far smaller than the workpiece size. In order to achieve a high stiffness, the bottom of the workpiece was completely fixed by glue contacts, where the nodes were constrained in both normal and tangential directions to the rigid wall. For the purpose of allowing material deformation at the left and the right ends, symmetry boundaries were set to the two sidewalls without separation from the rigid wall and friction with the rigid wall.

In figure 1, the rake angle and the relief angle of the tool were set to 0° and 10° , respectively. The tool edge radius was changed from 50 to 1000 nm, which covers the reported experimental ranges of tool edge radii. In order to avoid thermal effects, the cutting speed was set to 0.05 m s^{-1} , far lower than the experimental ranges [1–6]. The effect of cutting speed will be discussed elsewhere. In order to examine the effect of tool edge radius, we used the same depth of cut (100 nm) for all cuts. At this depth of cut, silicon tends to behave in a ductile manner, thus can be numerically modeled as a continuum.

Crystallographic effect is also an important factor in ductile machining of silicon. As has been experimentally demonstrated by previous studies [1–3, 6], the critical depth of cut for brittle–ductile transition is strongly dependent on workpiece crystal orientation. However, the crystallographic effect and the edge radius effect are two independent factors, that is, the basic trend of the edge radius effect does not depend

strongly on the crystal orientation of the workpiece. In this paper, we investigated the edge radius effect and did not put the crystallographic effect into the scope of study.

In this work, the Young's modulus of the workpiece was set to 202 GPa [26] which was an experimental value obtained by nanoindentation tests on undoped single-crystal silicon (100) at a maximum load of 15 mN and a corresponding depth of 267 nm. We used this value because the geometrical conditions used in the nanoindentation measurements were similar to those of the micro-cutting in this paper, although the theoretically calculated Young's modulus of silicon was somewhat lower [27]. The Poisson's ratio of the workpiece material was set to 0.3, which is an approximation of 0.279 obtained for {100} planes in (001) and (001) directions of silicon [27]. The approximation was performed by considering that Poisson's ratio increases remarkably with strain in silicon [28].

Material deformation in cutting is also influenced by tool-workpiece friction. There are two types of friction, namely, Coulomb friction and shear friction. The friction between the tool and chip in this work is of the shear type. Shear friction is typically used for applications like metal forming to limit the amount of friction due to plastic deformation. While the friction coefficient between diamond and silicon during cutting remains unknown with no literature available on the issue, in the present study we simply assumed that it was the same as that between a diamond indenter tip and silicon in scratching tests, namely, 0.05 [26].

2.2. The material model

Silicon has a strong directional covalent bonding with a diamond structure, thus at room temperature, dislocations are immobile and silicon responds in a brittle manner. Dislocations of silicon can only be activated at a high temperature ($>600^\circ$). Below this temperature, a high pressure might be the only approach for achieving ductility in silicon. It has been known that under a high hydrostatic pressure (10–16 GPa), such as in indentation tests, silicon will undergo phase transformations from the diamond cubic structure to a metallic phase (β -Sn) which is plastically deformable [29–35]. Therefore, in cutting, which is also a high-pressure process, we may roughly approximate the high-pressure phases of silicon as an elastic–plastic body. In this paper, we modeled silicon as an elastic–plastic body using the Johnson–Cook (JC) constitutive work flow stress model which has been widely used to characterize metal materials [36]. The JC model can be expressed by

$$\bar{\sigma} = [A + B(\bar{\epsilon})^n] \cdot \left[1 + C \ln \left(\frac{\dot{\bar{\epsilon}}}{\dot{\bar{\epsilon}}_0} \right) \right] \cdot \left[1 - \left(\frac{T - T_{\text{room}}}{T_{\text{melt}} - T_{\text{room}}} \right)^m \right], \quad (1)$$

where $\bar{\sigma}$ is the flow stress, and $\bar{\epsilon}$ is the plastic equivalent strain, T is the temperature, parameter A is the initial yield strength of the material at room temperature (T_{room}) and a strain rate of 1 s^{-1} ; strain rate $\dot{\bar{\epsilon}}$ is normalized with a reference strain rate $\dot{\bar{\epsilon}}_0$. The temperature term in the JC model reduces the flow

stress to zero at the melting temperature of the work material (T_{melt}), leaving the constitutive model with no temperature effect. In general, parameters A , B , C , n and m of the model are fitted to the data obtained by material tests conducted at low strains and strain rates, and at room temperature, as well as split Hopkinson pressure bar (SHPB) tests at strain rates up to 1000 s^{-1} and at temperatures up to 600°C .

2.3. The FE formulation model

Cutting is a typical large-strain process. For a large-strain problem, the constitutive relation must be defined in a correct frame of reference and be transformed from this reference frame to that in which the equilibrium equations are defined. Usually, two formulations can be used: the total Lagrangian formulation and the updated Lagrangian formulation [37, 38]. The theoretical difference between the two formulations lies in the choice of different reference configurations for the kinematic and static variables. In the total Lagrangian formulation, all static and kinematic variables are referred to the initial configuration, while in the updated Lagrangian formulation all static and kinematic variables are referred to the configuration of the previous step. Both the total Lagrangian and updated Lagrangian formulations include all kinematic nonlinear effects due to large displacement, large rotations and large strains, but whether the large strain behavior is modeled appropriately depends on the constitutive relations specified. The updated Lagrangian approach is especially useful in analyzing structures where inelastic behavior (plasticity, viscoplasticity and creep) causes the large deformations, and where rotations are so large that the nonlinear terms in the curvature expressions may no longer be neglected. It is suitable for large-strain plasticity analysis, where the plastic deformations cannot be assumed to be infinitesimal. In this work, the updated Lagrangian formulation was used by controlling strains and stresses at local coordinate frames at element integration points.

2.4. Remeshing criteria

Early works on FEM simulation of cutting processes were performed for steady-state cutting without considering chip separation [18, 19]. In later works, chip formation was performed by the separation criteria such as distance tolerance [20], strain energy density [21] and fracture mechanics-based parameters [22]. These chip separation criteria did not involve remeshing of the workpiece, thus might cause errors in chip deformation and chip flow characteristics. In a few recent works, remeshing was performed, but the remeshing criterion was based on a single parameter, such as penetration or angle distortion. The single-parameter criteria can reduce calculating time, but may cause process instability such as unexpected fluctuations in calculation results which do not occur in an actual machining process.

In the present study, the workpiece was remeshed by an adaptive remeshing method based on four remeshing criteria: strain change, element distortion, angle deviation and penetration, as schematically shown in figure 2.

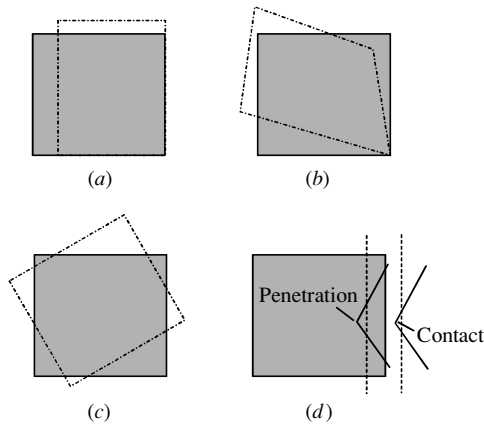


Figure 2. Schematic model for remeshing criteria: (a) strain change, (b) element distortion, (c) angle deviation and (d) penetration.

- (1) Strain change: a record of the strain change after remeshing is kept for each element. When any element of the body has a strain change greater than the control limit, the remeshing will start.
- (2) Element distortion: the identified body is remeshed when the distortion in the elements becomes larger than a critical value. In two-dimensional analysis, the distortion check is based on corner angles.
- (3) Angle deviation: remeshing is performed when any element has a change of angle greater than the input value.
- (4) Penetration: remeshing is performed if penetration between contact bodies is larger than two times the contact tolerance distance. Penetration is judged from the contact position between the tool and the workpiece. If the distance between the workpiece and the tool is smaller than one contact tolerance, which is by default 0.05 times the minimum length of an element edge, the two objects will be considered to be in contact.

The above four parameters were simultaneously monitored and the order of priority was compared. Whenever the predefined control limits of these parameters had been satisfied, the workpiece would be remeshed. In this way, the chip formation behavior can be predicted precisely, and the simulated results will be extremely close to the actual cutting process. This approach will also improve the accuracy of the simulation outputs, such as cutting forces and cutting temperatures.

2.5. Chip generation

Remeshing starts by creating elements along the boundary of the diamond tool. The new boundary front for the workpiece is then formed at the tool–chip interface. This front advances inward until the complete region is remeshed. This cycle is performed one time at each increment step of the tool, and continues until the whole workpiece is cut to form a chip. The element size can be changed gradually from the boundary to the interior allowing smaller elements near the boundary with no tying constraints necessary. The minimum element edge length after remeshing is set to 1 nm.

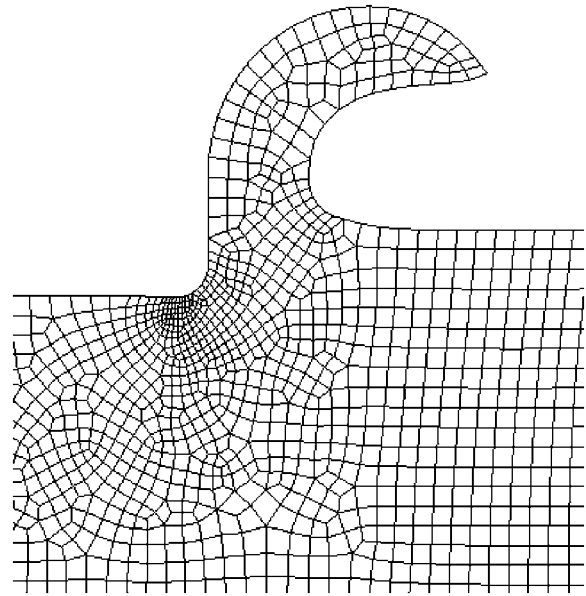


Figure 3. Snapshot of chip formation process realized by the proposed adaptive remeshing technique.

As the tool advances into the workpiece, the workpiece material is first pushed downward ahead of the tool and then flows upward along the rake face to form a sharp protrusion out of the uncut surface. The protrusion grows gradually and begins to separate from the rake face as a curled chip. Figure 3 shows a snapshot of the chip formation process when cutting with a tool having an edge radius of 50 nm. In the adaptive remeshing technique, the mesh density changes dynamically. High remeshing density is seen around the tool tip where the material deformation is significant.

3. Results and discussion

3.1. Cutting force

First, cutting force characteristics were investigated. Figures 4(a) and (b) show variations of the FEM-simulated cutting force components, namely, principal force and thrust force, during two cuts with tools having different edge radii, 100 nm and 200 nm, respectively. In both of the figures, cutting forces increase rapidly as the tool advances into the workpiece. After about 100 s in figure 4(a) and 150 s in figure 4(b), the forces tend to be constant, indicating a steady cutting state. It is noted that the forces in figure 4(b) are higher than those in figure 4(a). Moreover, in figure 4(a), the principal force is always higher than the thrust force, while in figure 4(b), the thrust force becomes bigger than the principal force after about 50 s from the beginning of the cut.

Figure 5(a) shows a plot of the cutting forces against the edge radius in the steady cutting state. The data points in the figure are the average forces during a period of time from the 200th to the 250th s in each cut. It can be seen that both the principal force and the thrust force increase proportionally with the edge radius. However, the slope of the increase in the thrust force is distinctly steeper than that

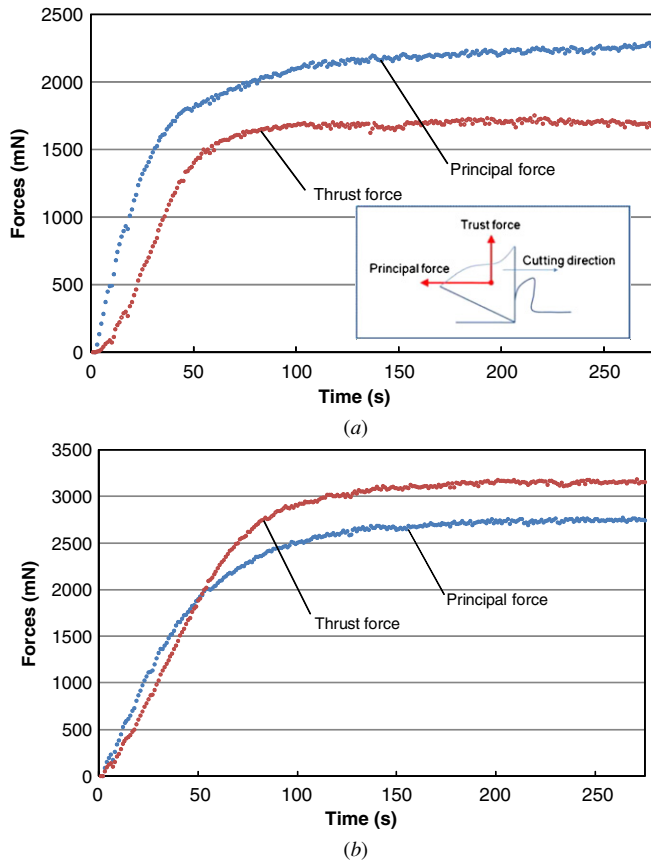


Figure 4. Variations of cutting forces during cutting with tools having different edge radii: (a) 100 nm, (b) 200 nm.

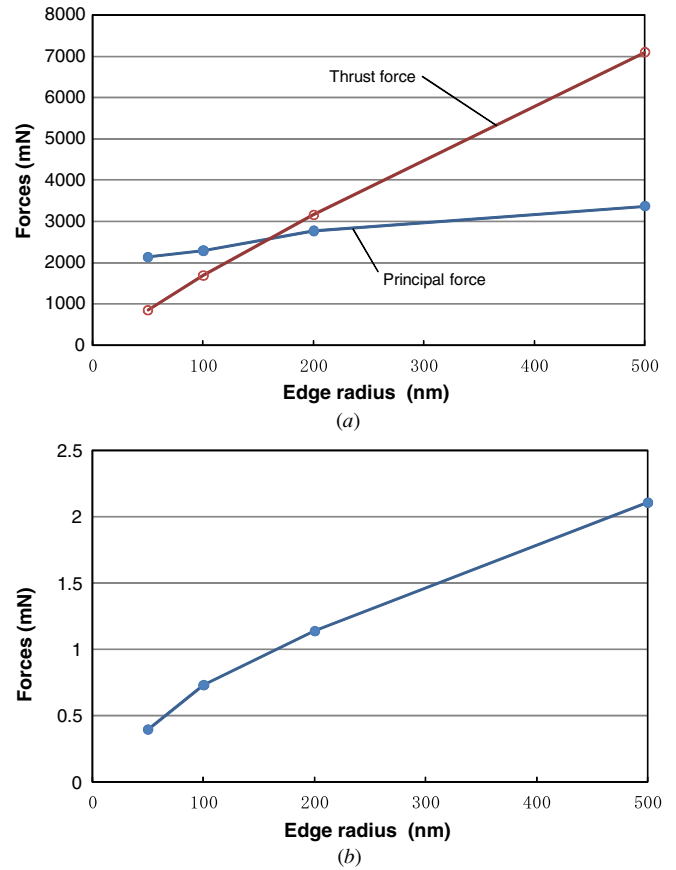


Figure 5. Plots of (a) cutting forces and (b) force ratio against tool edge radius in the steady cutting state.

of the principal force. Figure 5(b) is a plot of the force ratio (ratio of the thrust force and the principal force) against the edge radius. The force ratio also exhibits a nearly proportional increase with the edge radius. At a large edge radius of 500 nm, the force ratio becomes over 2.

3.2. Stress distribution

3.2.1. Von Mises stress. Figure 6 shows the distributions of the equivalent stress (Von Mises stress) in the cutting region at different edge radii from 50 nm to 500 nm. It can be seen that in figure 6(a), there are two high-stress regions. The first one (I) is around the tool tip, the area of which is very small. The second one (II) is long and narrow, oriented from below the tool tip to the free surface of the workpiece at an angle of about 45° to the cutting direction. The position of region II is roughly in accordance with the primary shear zone usually seen in traditional metal cutting. The highest value of the Von Mises stress reaches ~15 GPa in both of the two high-stress regions.

Compared with figure 6(a), in figure 6(b), the high-stress region I is obviously smaller while region II tends to expand downward into a deeper region of the workpiece. In figure 6(c), region I has disappeared while region II extends much deeper. In figure 6(d), region II becomes further deeper and broader, forming a large triangular high-stress region beneath/ahead of the tool. It can be clearly seen that from (a) to (d), the total

area of the high-stress region increases significantly with the tool edge radius.

Figure 7 is a plot of the maximum Von Mises stress in the cutting region against the tool edge radius. As the edge radius increases, the maximum stress decreases slightly, but is still maintained at a high level (~14 GPa).

3.2.2. Hydrostatic stress. Next, the hydrostatic stress component in the stress field was examined. Hydrostatic stress σ is the average of the three stress components in the three principal axes ($\sigma_1, \sigma_2, \sigma_3$) and can be described by

$$\sigma = \frac{1}{3}(\sigma_1 + \sigma_2 + \sigma_3). \quad (2)$$

The hydrostatic stress distributions in the cutting region at different edge radii are shown in figure 8. In figure 8(a), two regions of high compressive stress can be seen: one is just ahead of the tool tip (I'), and the other is near the boundary between the chip and the uncut surface (II'). The highest hydrostatic stress is ~-15 GPa, the absolute value of which is close to the Von Mises stress. This fact indicates that the hydrostatic pressure is dominant in the workpiece material while the deviatoric stress component is insignificant. As the edge radius increases (see figures 8(b)–(d)), the total area of the two regions, I' and II', increases too, and finally the two regions are combined into one.

These results strongly demonstrate that the necessary hydrostatic pressure for silicon phase transformation will

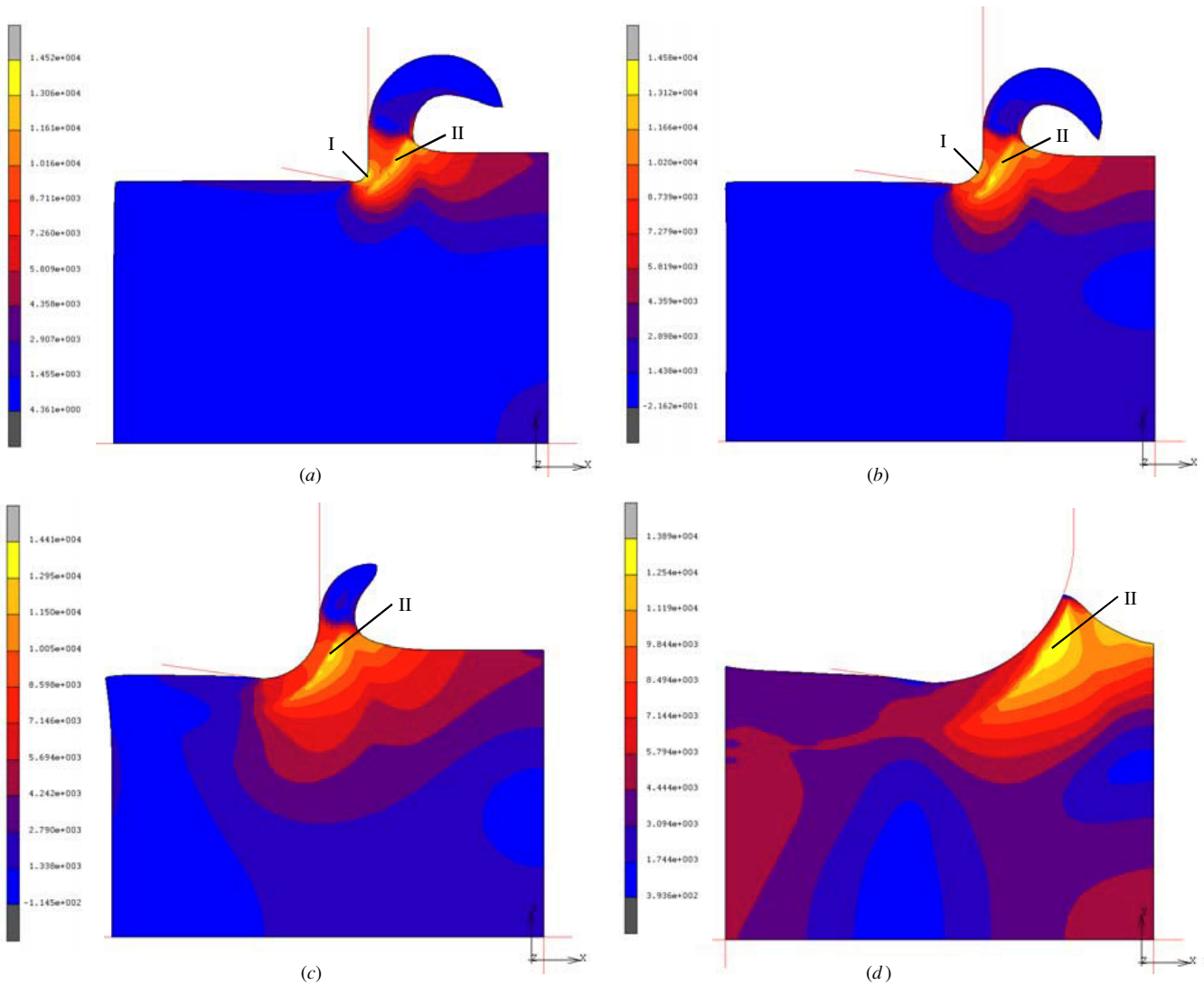


Figure 6. Variation in Von Mises stress distribution with tool edge radius: (a) 50 nm, (b) 100 nm, (c) 200 nm, (d) 500 nm.

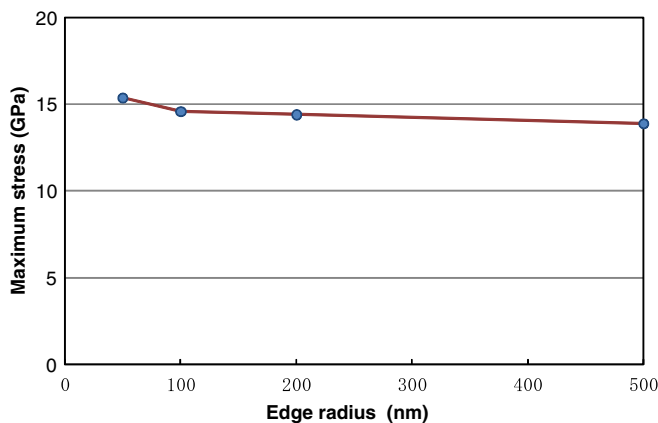


Figure 7. Variation in the maximum Von Mises stress with tool edge radius.

be readily generated in machining at the submicron scale. Increasing the tool edge radius (to ~500 nm) will expand the volume of the high-pressure metallic phase in the cutting

region, and in turn, improve the ductile response of silicon. This result agrees well qualitatively with the experimental results of Liu *et al* [17]. That is, the critical undeformed chip thickness increases linearly with the cutting edge radius in the range of 50–600 nm. It is presumable that in this range, the volume of the high-pressure metallic phase is directly related to the critical undeformed chip thickness for brittle–ductile transition.

3.3. Cutting temperature

Figure 9 shows temperature distributions in the cutting region. At an edge radius of 50 nm (figure 9(a)), a broad region of high temperature (R_1) can be seen near the boundary between the chip and the tool rake face. The workpiece material beneath the tool flank face (R_2) shows a slight temperature rise too, but the area of R_2 is remarkably smaller than that of R_1 . Other regions, including the high-stress regions (regions I and II in figure 6), do not exhibit significant temperature rise. This result demonstrates that the heat generation in silicon cutting is dominated by the friction between the tool and the

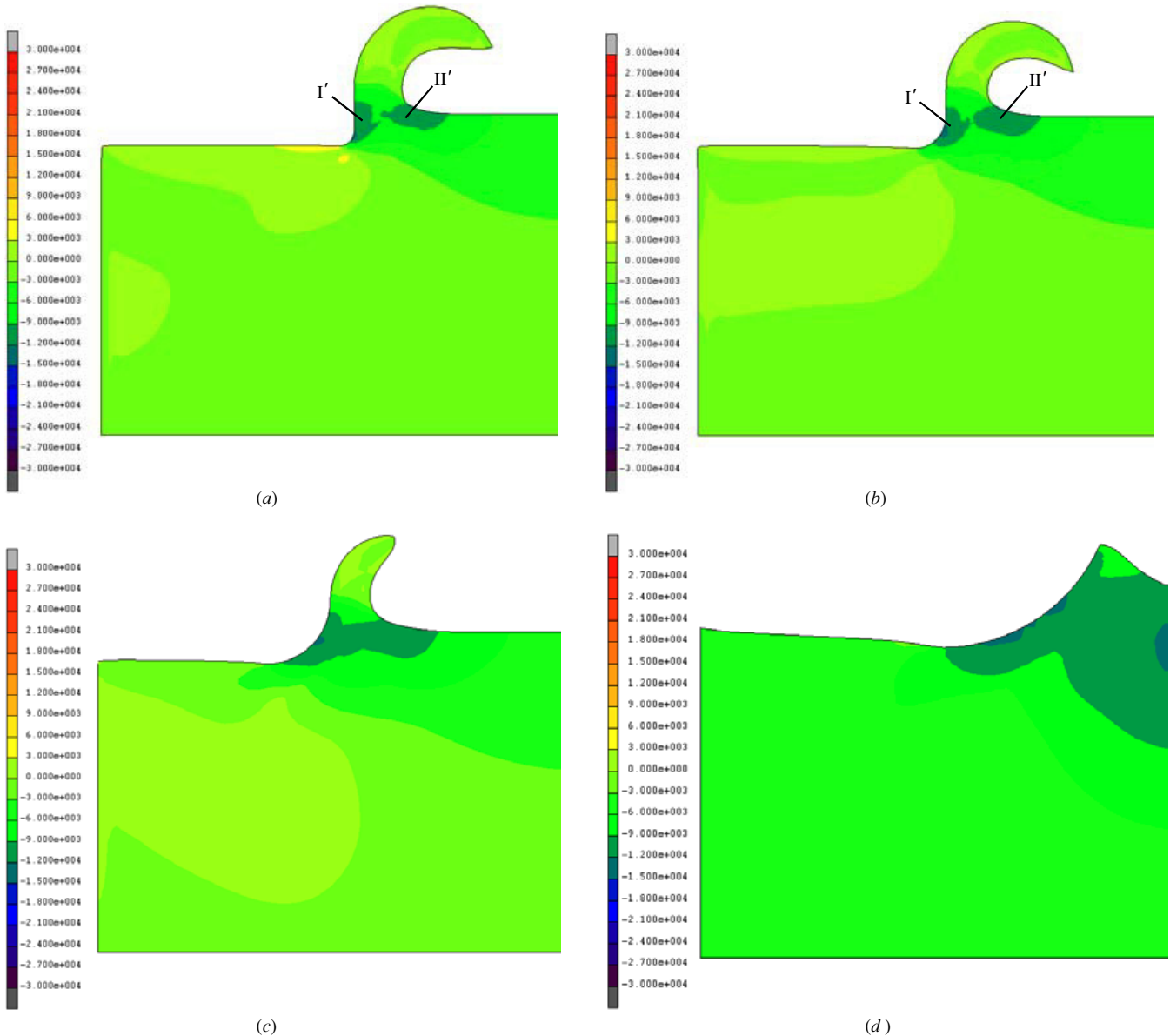


Figure 8. Hydrostatic stress distribution in the cutting region at different tool edge radii: (a) 50 nm, (b) 100 nm, (c) 200 nm, and (d) 500 nm.

workpiece material, rather than the material deformation inside the workpiece.

As the edge radius increases (see figures 9(b)–(d)), the high-temperature region in front of the tool rake face (R_1) shrinks, while that under the tool flank face (R_2) grows gradually. At an edge radius of 200 nm (figure 9(c)), the temperature rise at the flank face side has become higher than that at the rake face side. At an edge radius of 500 nm (figure 9(d)), temperature rise only takes places at the flank face side.

From the shifting of high-temperature zones, it is deduced that when cutting silicon with a sharp tool, crater wear will be predominant, while when using a dull tool, flank wear will become significant. The critical edge radius for this transition is between 100 and 200 nm. Compared with a crater wear, a flank wear will be a fatal limit for the service life of a diamond

tool [39]; hence, from the viewpoint of tool life, a tool edge radius smaller than 200 nm should be used.

Figure 10 is a plot of the highest temperature against the tool edge radius. It can be seen that the highest temperature is not strongly dependent on the edge radius. For all the edge radii, the maximum temperature is slightly above 300 °C. Since 300 °C is far lower than the melting point of silicon (1412 °C) and the temperature at which dislocation mobility of silicon may be activated (>600 °C), we can say that material softening due to the cutting heat is not a dominant reason for ductile material removal of silicon.

It should be pointed out that the cutting speed used in this paper is a low one (0.05 m s⁻¹). If a higher cutting speed is used, the cutting temperature should be higher too. For high-speed cutting, cutting heat generation might contribute to some extent to the ductile deformation of silicon. The effect of cutting speed will be discussed in detail elsewhere.

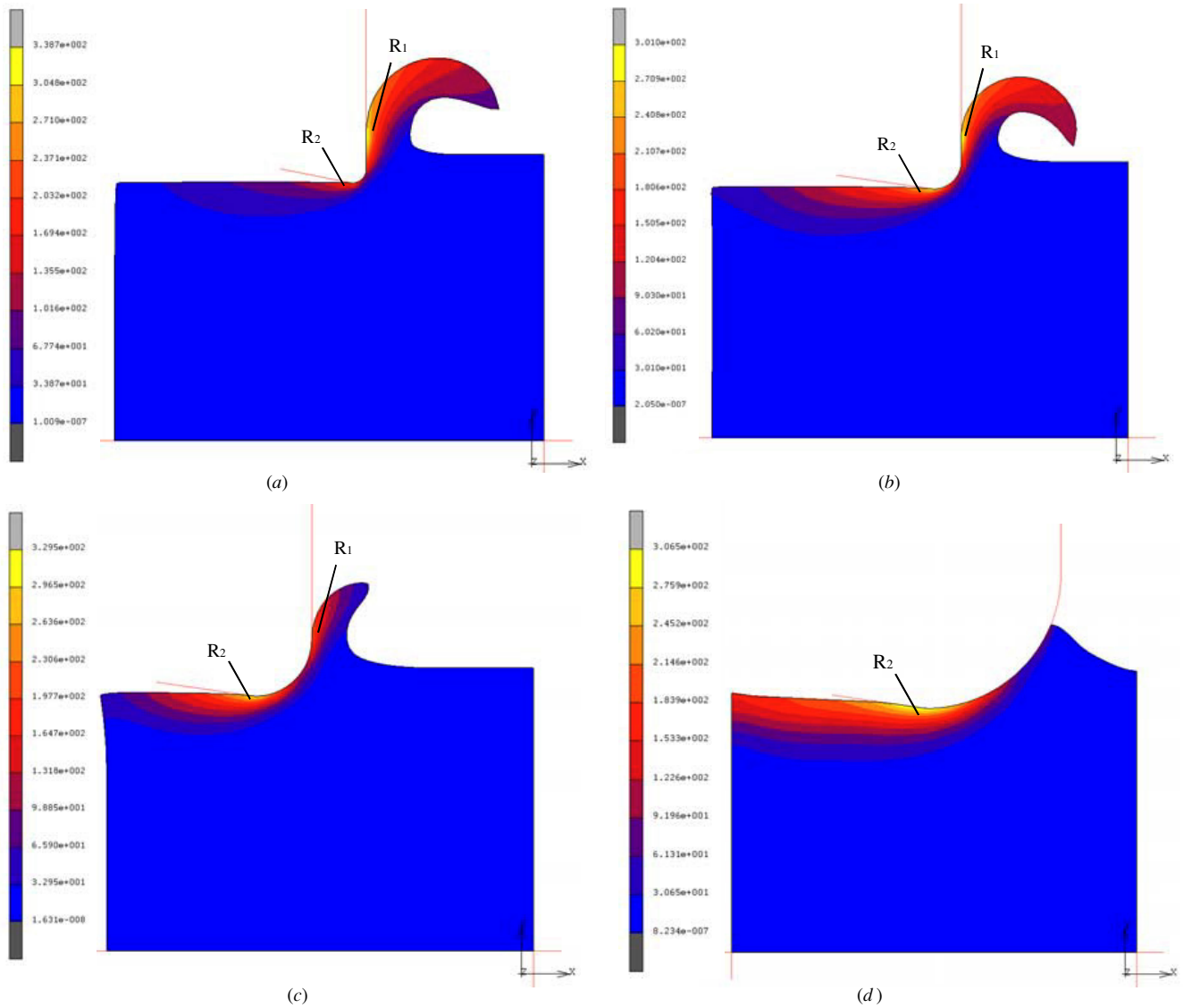


Figure 9. Temperature distribution in the cutting region at different tool edge radii: (a) 50 nm, (b) 100 nm, (c) 200 nm, and (d) 500 nm.

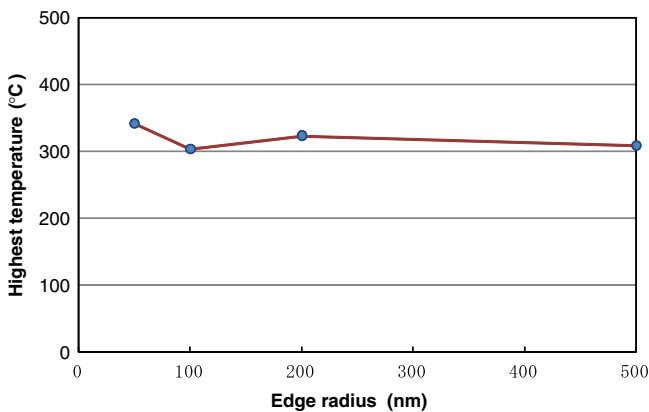


Figure 10. Variation in the highest cutting temperature with edge radius.

3.4. Chip formation

In figure 6 (also see figures 8 and 9), it is noteworthy that as the edge radius increases (from (a) to (c) in these figures), the

thickness of the generated chip decreases gradually. At an edge radius of 500 nm (d), there is only a small protrusion of material in front of the tool while no chip can be separated from the workpiece. When the tool advances further, the protrusion may grow gradually and finally form a small chip. However, chip formation in this case will be discontinuous and unsteady. The effective tool rake angle in this case is $\sim -76^\circ$.

Figure 11 shows the distributions of stress and temperature at an extremely large edge radius (1000 nm). Due to the highly negative effective rake angle ($\sim -83^\circ$) induced by the edge radius, material protrusion in front of the tool almost tends to vanish. Hence, even if the tool advances further at the same depth of cut, no chip formation will take place. In this case, the workpiece material flows downward along the tool edge profile and is then compressed into the bulk material beneath the tool. This situation is very similar to that of a burnishing process. Although burnishing is beneficial for metal materials because it generates a work-hardened subsurface layer in the workpiece, it is not advantageous for silicon. Instead of the work-hardening effects, silicon undergoes amorphization, leading to

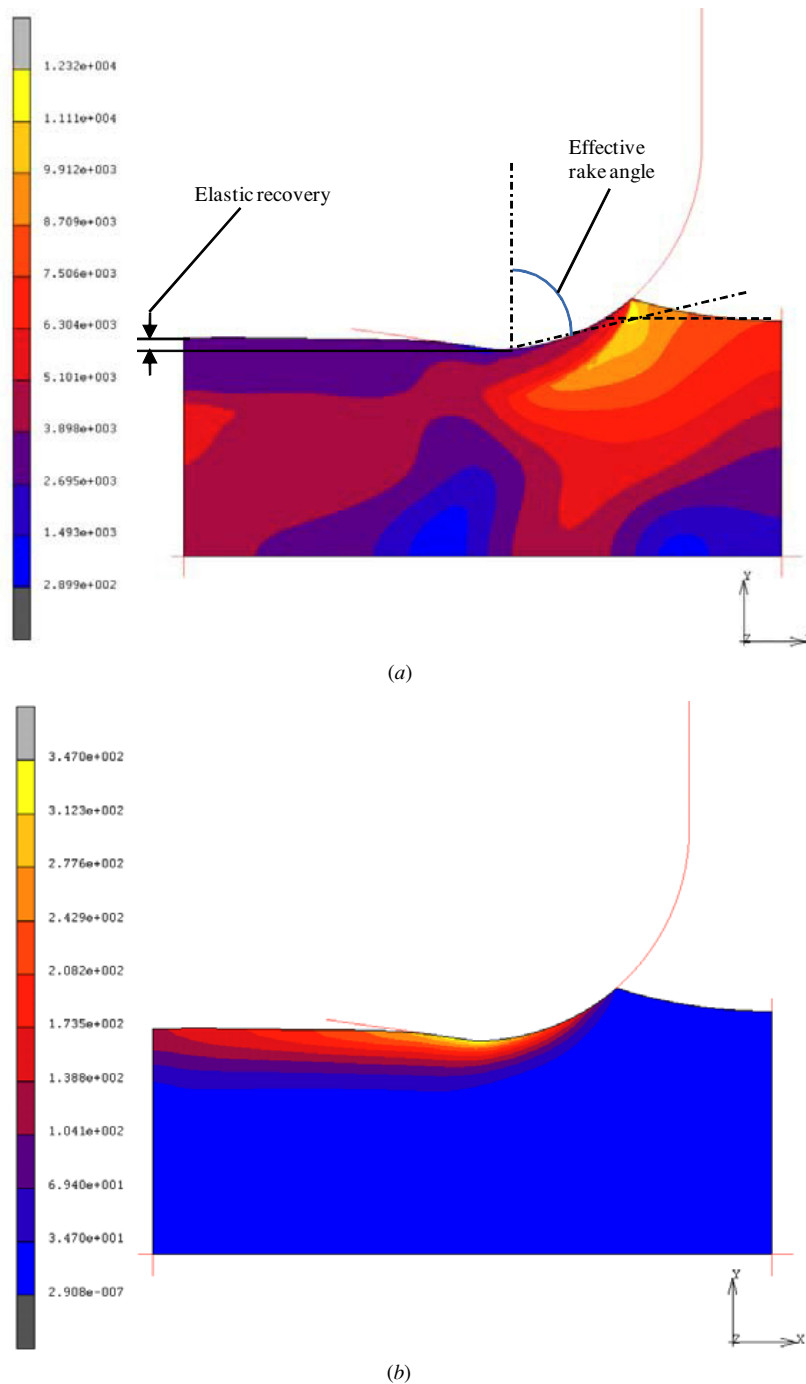


Figure 11. Distributions of (a) Von Mises stress and (b) temperature in the cutting region at an edge radius of 1000 nm.

a softened subsurface damage layer [11]. After the tool pass, the phase-transformed material will then undergo significant elastic recovery, leading to an error in the actual depth of cut. In figure 11, an elastic recovery of ~ 50 nm can be clearly seen, which is a half of the nominal depth of cut (100 nm). Furthermore, if the thickness of the downward flowing material is larger than a critical value, lateral cracks will take place after the tool passes due to the tensile stress occurring along the elastic/plastic boundary [13]. As an example, figure 12 shows a scanning electron microscope (SEM) micrograph of a used single-crystalline diamond tool with a large edge radius (~ 1000 nm). Long and deep wear marks are

clearly seen on the tool flank face, which is presumably caused by the severe friction between the tool and the elastically recovered workpiece material.

From the simulation results, it can be seen that optimization of tool edge radius is very important for ductile machining of silicon. The edge radius affects cutting force characteristics, cutting stress and temperature distribution, as well as chip formation. From the viewpoint of improving ductile response of silicon, a large edge radius is preferable (see figure 8). However, a large edge radius will cause an increase in cutting forces, especially the thrust force (see figures 4, 5), lead to a decrease in the effective depth of cut (figures 6, 8,

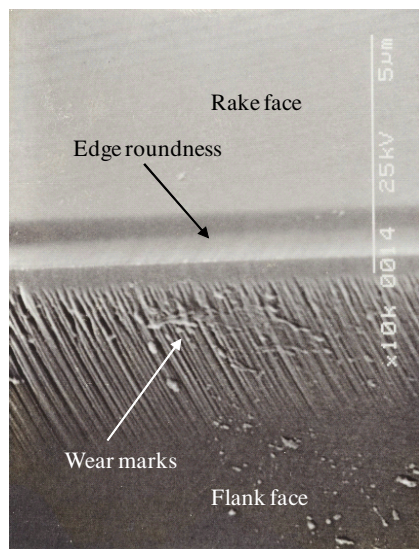


Figure 12. SEM micrograph of a used diamond tool having a large edge radius (~ 1000 nm), showing wear marks on the tool flank face.

9, 11) and give rise to a big dimensional error and a deep subsurface damage layer (figure 11). As subsurface damage is a crucial factor which degrades the product quality [40], sharp tools should be selected. On the basis of the simulation results from the present study, we propose that an edge radius smaller than 200 nm should be used for achieving both a good surface/subsurface integrity and a long tool life. The results from the present study might be also useful for optimizing the size of abrasive grains in silicon-wafer grinding processes, where the abrasive grains can be modeled as single-point tools with different edge radii.

4. Conclusions

Ductile cutting of silicon has been simulated by FEM based on a four-parameter adaptive remeshing technique. The effects of tool edge radius on cutting force, cutting stress and temperature, as well as chip formation have been investigated. The main conclusions can be summarized as:

- (1) Increasing the tool edge radius causes a significant increase in the cutting forces, especially the thrust force. The force ratio can be over 2 if a very dull tool is used.
- (2) As the edge radius increases, the region under high equivalent stress expands and moves downward and forward away from the tool tip.
- (3) A hydrostatic pressure up to ~ 15 GPa is generated in the cutting region, which is sufficiently high to cause phase transformations in silicon. As the edge radius increases, the volume of the material under high pressure increases too.
- (4) Temperature rise occurs intensively near the tool-chip interface. Under the present low-speed cutting conditions, the highest temperature (~ 300 °C) is far lower than the temperature at which dislocation mobility of silicon can be activated (> 600 °C).
- (5) As the edge radius increases, the primary high-temperature zone shifts from the rake face side to the

flank face side, which will cause a change in tool wear pattern from crater wear to flank wear. The critical edge radius for the transition is about 200 nm.

- (6) Increasing the edge radius leads to a decrease in the effective depth of cut and an increase in elastic recovery of material. Continuous chip formation cannot be realized when the edge radius is over 500 nm. An edge radius smaller than 200 nm is recommended.

References

- [1] Blake P N and Scattergood R O 1990 Ductile regime machining of germanium and silicon *J. Am. Ceram. Soc.* **73** 949–57
- [2] Nakasuji T, Kodera S, Hara S, Matsunaga H, Ikawa N and Shimada S 1990 Diamond turning of brittle materials for optical components *Ann. CIRP* **39** 89–92
- [3] Shibata T, Fujii S, Makino E and Ikeda M 1996 Ductile-regime turning mechanism of single-crystal silicon *Precis. Eng.* **18** 130–7
- [4] Yan J, Syoji K and Kuriyagawa T 1999 Chip morphology of ultraprecision diamond turning of single crystal silicon *J. Japan Soc. Precis. Eng.* **65** 1008–12
- [5] Yan J, Yoshino M, Kuriyagawa T, Shirakashi T, Syoji K and Komanduri R 2001 On the ductile machining of silicon for micro electro-mechanical systems (MEMS), opto-electronic and optical applications *Mater. Sci. Eng. A* **297** 230–4
- [6] Yan J, Syoji K, Kuriyagawa T and Suzuki H 2002 Ductile regime turning at large tool feed *J. Mater. Process. Technol.* **121** 363–72
- [7] Shibata T, Ono A, Kurihara K, Makino E and Ikeda M 1994 Cross-section transmission electron microscope observations of diamond-turned single-crystal Si surfaces *Appl. Phys. Lett.* **65** 2553–5
- [8] Morris J C, Callahan D L, Kulik J, Patten J A and Scattergood R O 1995 Origins of the ductile regime in single-point diamond turning of semiconductors *J. Am. Ceram. Soc.* **78** 2015–20
- [9] Gogotsi Y, Baek C and Kirscht F 1999 Raman microspectroscopy study of processing-induced phase transformations and residual stress in silicon *Semicond. Sci. Technol.* **14** 936–44
- [10] Yan J 2004 Laser micro-Raman spectroscopy of single-point diamond machined silicon substrates *J. Appl. Phys.* **95** 2094–101
- [11] Yan J, Takahashi H, Tamaki J, Gai X, Harada H and Patten J 2005 Nanoindentation tests on diamond-machined silicon wafers *Appl. Phys. Lett.* **86** 181913
- [12] Yan J, Asami T and Kuriyagawa T 2008 Nondestructive measurement of machining-induced amorphous layers in single-crystal silicon by laser micro-Raman spectroscopy *Precis. Eng.* **32** 186–95
- [13] Yan J, Syoji K and Kuriyagawa T 1999 Effects of cutting edge geometry on brittle-ductile transition in silicon machining *Precision Science and Technology for Perfect Surface Proc. 9th International Conf. on Precision Engineering (ICPE)* ed Y Furukawa, Y Mori and T Kataoka (: Japan Society for Precision Engineering) pp 92–7
- [14] Fang F Z and Zhang G X 2003 An experimental study of edge radius effect on cutting single crystal silicon *Int. J. Adv. Manuf. Technol.* **22** 703–7
- [15] Patten J A and Gao W 2001 Extreme negative rake angle technique for single point diamond nano-cutting of silicon *Precis. Eng.* **25** 165–7
- [16] Arefin S, Li X P, Cai M B, Rahman M, Liu K and Tay A A O 2007 Effect of cutting edge radius on machined surface in

- nanoscale ductile mode cutting of silicon wafer *Proc. Inst. Mech. Eng. B* **221** 213–20
- [17] Liu K, Li X P, Rahman M, Neo K S and Liu X D 2007 A study of the effect of tool cutting edge radius on ductile cutting of silicon wafers *Int. J. Adv. Manuf. Technol.* **32** 631–7
- [18] Iwata K, Osakada K and Terasaka Y 1984 Process modeling of orthogonal cutting by the rigid-plastic finite element method *J. Eng. Mater. Technol.* **106** 132–8
- [19] Strenkowski J S and Carroll J T 1985 A finite element model of orthogonal metal cutting *J. Eng. Ind.* **107** 347–54
- [20] Komvopoulos K and Erpenbeck S A 1991 Finite element modeling of orthogonal metal cutting *J. Eng. Ind.* **113** 253–67
- [21] Lin Z C and Lin S Y 1992 A coupled finite element model of thermoelastic–plastic large deformation for orthogonal cutting *J. Eng. Mater. Technol.* **114** 218–26
- [22] Hashemi J, Tseng A A and Chou P C 1994 Finite element modeling of continuous and segmental chip formation in high speed orthogonal machining *J. Mater. Eng. Perform.* **3** 712–21
- [23] Bil H, Kilic S E and Tekkaya A E 2004 A comparison of orthogonal cutting data from experiments with three different finite element models *Int. J. Mach. Tools Manuf.* **44** 933–44
- [24] Ee K C, Dillon O W Jr and Jawahir I S 2005 Finite element modeling of residual stresses in machining induced by cutting using a tool with finite edge radius *Int. J. Mech. Sci.* **47** 1611–28
- [25] Woon K S, Rahman M, Fang F Z, Neo K S and Liu K 2008 Investigations of tool edge radius effect in micromachining: a FEM simulation approach *J. Mater. Process. Technol.* **195** 204–11
- [26] Bhushan B and Li X 1997 Micromechanical and tribological characterization of doped single-crystal silicon and polysilicon films for microelectromechanical systems devices *J. Mater. Res.* **12** 54–63
- [27] Brantley W A 1973 Calculated elastic constants for stress problems associated with semiconductor devices *J. Appl. Phys.* **44** 534–5
- [28] Zhu R, Pan E, Chung P W, Cai X, Liew K M and Buldum A 2006 Atomistic calculation of elastic moduli in strained silicon *Semicond. Sci. Technol.* **21** 906–11
- [29] Gridneva I V, Milman Y V and Trefilov V I 1972 Phase transition in diamond-structure crystals during hardness measurements *Phys. Status Solidi a* **14** 177–182
- [30] Pharr G M, Oliver W C and Harding D S 1991 New evidence for a pressure-induced phase transformation during the indentation of silicon *J. Mater. Res.* **6** 1129–30
- [31] Kailer A, Gogotsi Y G and Nickel K G 1997 Phase transformations of silicon caused by contact loading *J. Appl. Phys.* **81** 3057–63
- [32] Bradby J E, Williams J S, Wong-Leung J, Swain M V and Munroe P 2000 Transmission electron microscopy observation of deformation microstructure under spherical indentation in silicon *Appl. Phys. Lett.* **77** 3749–51
- [33] Zarudi I, Zou J and Zhang L C 2003 Microstructures of phases in indented silicon: a high resolution characterization *Appl. Phys. Lett.* **82** 874–6
- [34] Yan J, Takahashi H, Tamaki J, Gai X and Kuriyagawa T 2005 Transmission electron microscopic observation of nanoindentations made on ductile-machined silicon wafers *Appl. Phys. Lett.* **87** 211901
- [35] Yan J, Takahashi H, Gai X, Harada H, Tamaki J and Kuriyagawa T 2006 Load effects on the phase transformation of single-crystal silicon during nanoindentation tests *Mater. Sci. Eng. A* **423** 19–23
- [36] Umbrello D, M'Saoubi R and Outeiro J C 2007 The influence of Johnson–Cook material constants on finite element simulation of machining of AISI 316L steel *Int. J. Mach. Tools Manuf.* **47** 462–70
- [37] Noguchi H and Hisada T 1995 Integrated FEM formulation for total/updated-lagrangian method in geometrically nonlinear problems *JSME Int. J. A* **38** 23–9
- [38] Yen Y C, Jain A and Altan T 2004 A finite element analysis of orthogonal machining using different tool edge geometries *J. Mater. Process. Technol.* **146** 72–81
- [39] Yan J, Syoji K and Tamaki J 2003 Some observations on the wear of diamond tools in ultra-precision cutting of single-crystal silicon *Wear* **255** 1380–7
- [40] Yan J, Asami T, Harada H and Kuriyagawa T 2008 Fundamental investigation of subsurface damage in single crystalline silicon caused by diamond machining *Precis. Eng.* doi:10.1016/j.precisioneng.2008.10.008 at press